Design of Ultra-High-Speed Motor for FCEV Air Compressor Considering Mechanical Properties of Rotor Materials

Jae-Hyun Kim, Dong-Min Kim, *Member, IEEE*, Young-Hoon Jung, and Myung-Seop Lim

***Abstract*—This paper proposes the design process of an ultra-high-speed surface-mounted permanent magnet synchronous motor for a fuel-cell electric vehicle air compressor. Proposed design process enables ultra-high-speed motor design while considering mechanical stresses of the rotor materials according to the temperature. In the rotor design stage, the worst temperature condition of the permanent magnet and retaining sleeve on mechanical stress is investigated and reflected using analytical method. Rotor dimension such as permanent magnet and retaining sleeve thickness is determined considering both electromagnetic performance and mechanical characteristics. Then, from the initially designed model, the eddy current loss according to the shape ratio (SR) and torque density (TD) is analytically derived using proportional equation and finite-element analysis result. Then, SR and TD to reduce the eddy current loss and maximize the efficiency are determined while considering the first bending critical speed. Finally, to verify the proposed design process, the prototype is fabricated and tested. Test results show good agreement with the finite-element analysis results, and it is confirmed that the rotor is operated at the highest rotational speed without mechanical failure.**

***Index Terms*—Critical speed, eddy current loss, fuel cell electric vehicle (FCEV), retaining sleeve, surface-mounted permanent magnet synchronous motor (SPMSM), ultra-high-speed motor.**

I. Introduction

RECENTLY, fuel cell electric vehicles (FCEV) are receiving attention for commercialization. As a way to surpass the laboratory level and achieve commercialization, it is necessary to address the issue of high weight. To realize this, the weight of the cell stack must be reduced. In order to make the cell stack light, the supplied oxygen pressure and the flow rate must be increased. As solution, a centrifugal compressor type using an electric motor has been proposed [1]–[3]. In this case, as the rotational speed and output power of the motor for air compressor increase, the weight of the FCEV can be reduced.

Surface-mounted permanent magnet synchronous motors (SPMSMs) with shrink-fitting retaining sleeve are widely used for ultra-high-speed motors, due to its simple configuration [4]. However, important design considerations exist when designing a SPMSM for ultra-high-speed application as follows: 1) mechanical stress of the rotor, 2) eddy current loss of the rotor 3) critical speeds. The mechanical stress of the rotor must be considered because of its high-speed operation which generates high centrifugal force [5]–[9]. Also, eddy current loss of the permanent magnet (PM) and retaining sleeve should be considered in design stage since it causes high temperature of the rotor, which can degrade the motor performance and induce demagnetization of PM [10]. In addition, rotor design while considering the first bending critical speed is essential since the rotor can mechanically fail if the operating speed range includes the critical speed [11] and [12].

Therefore, many researches have been conducted about these considerations. In [13], an ultra-high-speed slotless PM motor was designed using the analytical approach in consideration of rotor mechanical stress. Multiphysics optimization was carried out by simultaneously considering the torque, losses, and mechanical stress of the rotor. However, the eddy current losses of the PM and retaining sleeve were not considered, and the critical speeds of the rotor was not considered. Huang and Fang studied the multi-physics design and optimization of a high-speed PM motor while considering the mechanical stability and rotor eddy current loss in [14]. They determined the outer diameter of the PM in consideration of the electromagnetic performance, and only optimized the retaining sleeve thickness. However, the mechanical stress of PM and airgap length is changed when the retaining sleeve thickness is changed. Therefore, it is desirable to optimize the PM thickness and retaining sleeve thickness simultaneously considering electromagnetic performance and mechanical characteristics. In [15], the design process of 2-pole 6-slot high-speed machine was proposed and verified through a test. The design process included all the considerations of the rotor mechanical stress, eddy current loss, and critical speeds. However, when calculating the stress of the PM and retaining sleeve, only the maximum operable temperature of the PM was considered. Depending on the material of each part of the rotor,

Manuscript received July 4, 2020; revised October 13, 2020 and January 22, 2021; accepted February 22, 2021. Date of publication March 1, 2021; date of current version November 23, 2021. This work was supported by the Ministry of Trade, Industry, and Energy (MOTIE), Korea, under the 'Commercializing fuel cell electric vehicle component industry and R&D Support Program' (reference number R0006468) supervised by the Korea Institute for Advancement of Technology (KIAT). Paper no. TEC-00676-2020. *(Corresponding author: Myung-Seop Lim.)*

Jae-Hyun Kim, Dong-Min Kim, and Myung-Seop Lim are with the Department of Automotive Engineering, Hanyang University, Seoul 04763, Republic of Korea (e-mail: zerg1258@hanyang.ac.kr; kimdmin@hanyang.ac.kr; myungseop@hanyang.ac.kr).

Young-Hoon Jung is with the R&D Division, Hyundai Motor Company, Hwaseong 18280, Korea (e-mail: yh.jung@hyundai.com).

Color versions of one or more figures in this article are available at https://doi.org/10.1109/TEC.2021.3062646.

Digital Object Identifier 10.1109/TEC.2021.3062646

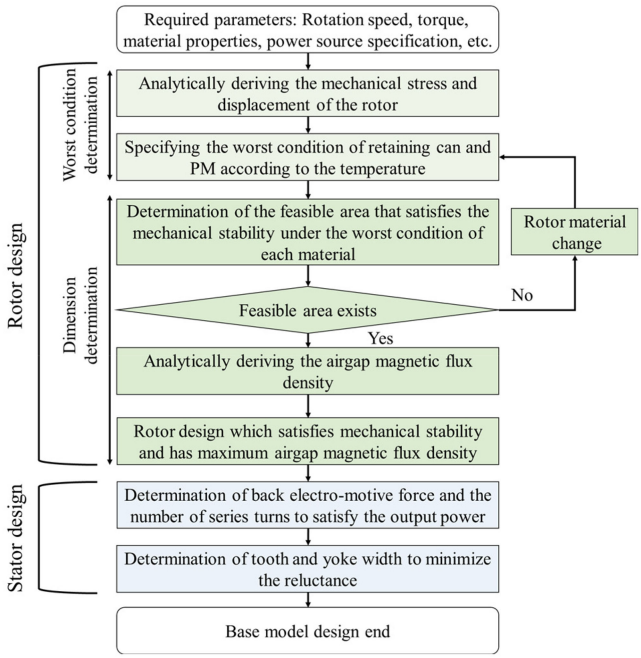

Fig. 1. Flow chart of ultra-high-speed SPMSM design procedure of the base model.

it cannot be assured whether the rotor will be vulnerable at low temperature or at high temperature.

This paper presents the design of an ultra-high-speed SPMSM for FCEV compressor while considering the mechanical stability and rotor eddy current loss. Since the PM and retaining sleeve are brittle and ductile material, respectively, the mechanical stress change according to the temperature of each material is different. Therefore, in this paper, the temperature condition with higher mechanical stress of each material is defined as the worst condition. Then, the rotor is designed in consideration of both electromagnetic performance and mechanical characteristics. The base model is then determined by designing the stator in consideration of the power specification and target output power, and this process is shown in Fig. 1. Then, the eddy current loss of the PM and retaining sleeve is analytically modeled using the proportional formula according to the shape ratio (SR) and torque density (TD). Considering the critical speed, improved model, which is called sizing model, with reduced eddy current loss was designed, and the performance was verified through a test.

The two main contributions of this paper are as follows: First, a rotor design process while considering mechanical stress by reflecting the worst temperature condition of brittle material (PM) and ductile material (retaining sleeve) is proposed. In general, the rotor is designed by considering only the rotor mechanical stress at high temperature condition [9] and [15]. However, the stress may be the highest at low temperature depending on the material. Therefore, it is essential to design the rotor in consideration of the worst temperature conditions for each material, and its effectiveness is described in Section IV-B. Second, a proportional formulation of the eddy current loss in PM and retaining sleeve according to SR and TD is proposed,

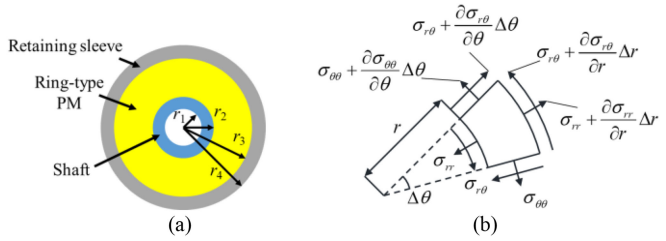

Fig. 2. (a) Configuration of the rotor. (b) Free body diagram of differential area with axisymmetric condition.

and the eddy current loss reduction design was carried out by utilizing this formulation. By analytically modeling the rotor eddy loss, the eddy current loss according to the motor size change can be calculated using only the finite element analysis (FEA) results of the base model. By doing so, designing time can be greatly reduced because the 3-D FEA according to the size of the motor is unnecessary.

This paper is organized as follows. In Section II, the base model of the ultra-high-speed SPMSM with a rotational speed of 110 krpm and output power of 14.4 kW is designed using the analytical method. Next, in Section III, the change in characteristics such as current density, line to line voltage, eddy current loss and efficiency according to the SR and TD are investigated via a combination of formulated proportional relations and finite element analysis (FEA), and a sizing model is derived [16]. In Section IV, fabrication of the sizing model with SR and TD that provides the highest efficiency with a reduced eddy current loss is detailed. A test was then conducted to verify the proposed design procedure. Also, effectiveness of the proposed rotor design process is verified.

II. Base Model Design Through Analytical Method

A. Rotor Design

1) Determination of Mechanically Stable Design Region: In the ultra-high-speed SPMSM, the PM can be scattered by the centrifugal force during high speed operation. Therefore, the PM is manufactured by shrink-fitting it into the retaining sleeve. The mechanical stress acting on the PM and the retaining sleeve owing to the centrifugal force and shrink-fitting can be greater than the yield stress. Thus, it is essential to design the rotor while considering the mechanical stress. In this section, the rotor was designed by analytically calculating the displacement and the stress acting on the PM and the retaining sleeve.

The structure of the rotor is shown in Fig. 2(a), consisting of hollow shaft, ring-shaped PM, which is segmented into two segments both axially and circumferentially to reduce eddy current loss, and retaining sleeve. The mechanical properties of the materials used in the rotor are listed in Table I. For PM material, Sm2Co17 is selected since the performance such as demagnetization characteristic at high temperature of Sm2Co17 is better than that of NdFeB PM. For retaining sleeve material, Inconel718 is selected since it has high yield strength and tensile strength, even at high temperatures. Also, since Inconel718 is a

TABLE I
MECHANICAL PROPERTIES OF ROTOR MATERIALS

Material	SUS630 (Shaft)	Sm2Co17 (PM)	Inconel718 (Sleeve)
Density (kg/m^3)	7750	8400	8190
Poisson's ratio	0.27	0.27	0.294
Young's modulus (GPa)	196	151	211
Yield strength (MPa)	1000	42 (tensile) 900 (compressive)	1036
Dilatation coefficient ($\times 10^{-6}$/°C)	10.8	9.6	13.5

TABLE II
GENERAL SOLUTIONS AND BOUNDARY CONDITIONS

Item	Equation
Radial displacement	$u_{rl} = A_l r + \frac{B_l}{r} - (1-\nu_l^2)\frac{\rho_l r^3 \omega^2}{8E_l}$
Radial-direction stress	$\sigma_{rrl} = \frac{E_l}{1-\nu_l} A_l - \frac{E_l}{1+\nu_l}\frac{B_l}{r^2} - \frac{3+\nu_l}{8}\rho_l r^2 \omega^2$
Circumferential-direction stress	$\sigma_{\theta\theta l} = \frac{E_l}{1-\nu_l} A_l + \frac{E_l}{1+\nu_l}\frac{B_l}{r^2} - \frac{1+3\nu_l}{8}\rho_l r^2 \omega^2$
Boundary conditions	$\sigma_{rrFE}(r_1) = 0$
	$\sigma_{rrPM}(r_2) = \sigma_{rrFE}(r_2) = p_1$
	$u_{rPM}(r_2) - u_{rFE}(r_2) = r_2(C_{FE} - C_{PM})(T - T_0)$
	$\sigma_{rrS}(r_3) = \sigma_{rrPM}(r_3) = p_2$
	$u_{rS}(r_3) - u_{rPM}(r_3) = \delta + r_3(C_{PM} - C_S)(T - T_0)$
	$\sigma_{rrS}(r_4) = 0$

non-magnetic material, it does not form a leakage magnetic flux path [4].

In order to analytically derive the stress and displacement of the cylindrical rotor shown in Fig. 2(a), the equilibrium equation of the differential area should be solved. Here, segmented PM is assumed as the integral cylinder. For the differential area in the cylindrical coordinate system with axisymmetric condition, the stress on the differential area could be formulated from the equilibrium equation which is depicted in Fig. 2(b). The general solution of displacement, radial-direction stress, circumferential-direction stress and boundary conditions at the radial position r are shown in Table II. Here, A and B are the undetermined coefficients, r is the radial position, ω is the rotational speed, u is the displacement, σ is the stress, E is the Young's modulus, ν is the Poisson's ratio, δ is the interference between PM and sleeve, T is the temperature, T_0 is the ambient temperature, and C is the dilatation coefficient. The subscripts r and rr denote the radial direction component, $\theta\theta$ denotes the circumferential direction component, and FE, PM and S denote the shaft, PM, and retaining sleeve, respectively.

From the general solutions and boundary conditions in Table II, undetermined coefficients A_l and B_l were calculated as (1) shown at the bottom of the next page.

Here, effect of the shrink-fitting is considered by reflecting the interference δ term in the boundary condition. Then, from the calculated undetermined coefficients A_l and B_l, specific solutions of radial-direction stress and circumferential-direction stress were calculated. From the calculated stress, the safety factor which is the ratio of the strength to the actual applied load of the PM and the retaining sleeve were calculated. When calculating the safety factor, for a ductile material such as shaft and retaining sleeve, the von-Mises theory was applied, and for a brittle material such as PM, the modified Mohr theory was applied as shown in Fig. 3 and Table III [17]. Here, n is the safety factor, S_y is the yield strength, σ_A and σ_B are the maximum and minimum principal stress, respectively. S_{uc} and S_{ut} are the compressive and tensile ultimate strength, respectively.

TABLE III
FAILURE THEORY OF DUCTILE AND BRITTLE MATERIAL

Item	Equation
von-Mises theory	$n = \frac{S_y}{(\sigma_A^2 - \sigma_A\sigma_B + \sigma_B^2)^{\frac{1}{2}}}$
modified Mohr theory	$n = \frac{S_{ut}}{\sigma_A}$ when $\sigma_A > \sigma_B \geq 0$
	$\sigma_A \geq 0 \geq \sigma_B$ and $\left\lvert\frac{\sigma_B}{\sigma_A}\right\rvert \leq 1$
	$n = \frac{S_{uc}S_{ut}}{(S_{uc} - S_{ut})\sigma_A - S_{ut}\sigma_B}$ when $\sigma_A \geq 0 \geq \sigma_B$
	and $\left\lvert\frac{\sigma_B}{\sigma_A}\right\rvert > 1$
	$n = -\frac{S_{uc}}{\sigma_B}$ when $0 \geq \sigma_A \geq \sigma_B$

Since the safety factors of PM and retaining sleeve vary with temperature, the rotor should be designed to be mechanically safe at the worst temperature condition. However, because PM is a brittle material and retaining sleeve is a ductile material, the worst conditions of each material must be identified and reflected in the rotor design. Thus, the safety factors of the retaining sleeve and the PM were analyzed according to the temperature to determine the worst condition of each material. Here, the safety factor was calculated with a 15% additional speed margin over the maximum operating speed of 110 krpm and the interference between the PM and retaining sleeve is 0.08 mm, and the shaft inner radius and shaft thickness are 3.0 mm and 2.0 mm, respectively. These parameters were determined by considering productivity and cooling conditions. The safety factor was obtained in the temperature range of −40 to 160 °C, which is the temperature range in which the motor should be operated without the occurrence of failure. Fig. 4 presents the safety factor tendency according to the temperature. For the retaining sleeve, as the temperature decreases, the mechanically stable region, where a safety factor is greater than 1.3, decreases. However, for the PM, as the temperature increases, the mechanically stable region decreases. Therefore, the worst conditions of the retaining sleeve and PM are at the lowest and highest temperatures, respectively. Under the worst condition of each material, the mechanically stable region where the safety factor is equal to or greater than 1.3 is presented in Fig. 5.

Then, in order to validate analytically calculated safety factor, a structural FEA was performed using ANSYS. The analysis was performed under the worst condition of each material as mentioned earlier; temperature of PM and retaining sleeve were

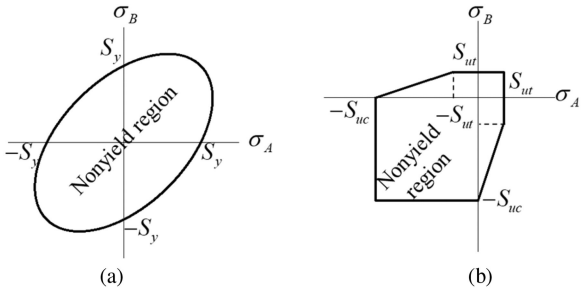

Fig. 3. Failure theory of ductile and brittle material. (a) Von-Mises theory. (b) Modified Mohr theory.

160 °C and −40 °C, respectively. Fig 6 shows the safety factor 1.3 line of PM and retaining sleeve obtained by FEA and analytical model. As can be shown in Fig. 6, analytical results agree well with the FEA result.

2) Airgap Magnetic Flux Density: To calculate the electromagnetic characteristics according to the dimension of the rotor, space harmonic analysis (SHA) was used [18]. SHA is the analytical technique used to obtain the magnetic scalar potential. Using magnetic scalar potential, the airgap magnetic flux density is calculated according to the dimension of the rotor with airgap length 1.4 mm, as shown in Fig. 7. Depending on the airgap length, characteristics such as torque, overall loss and mechanical stability have a trade-off relationship. However, in this study, the airgap length was determined in consideration of mechanical problem such as clearance of the air foil bearing.

3) Determination of Rotor Dimensions: The rotor dimensions were determined based on the safety factor and airgap magnetic flux density. The rotor was designed at the point of maximum airgap magnetic flux density in mechanically stable region as shown in Fig. 7. The resulting dimensions of the rotor were an inner shaft radius of 3.0 mm, a shaft thickness of 2.0 mm, PM thickness of 6.3 mm, and retaining sleeve thickness of 1.7 mm. The analytically calculated safety factors of the retaining sleeve and PM at the worst condition were 1.31 and 1.40, respectively. The safety factor at the worst condition for each material and the specifications of the designed rotor are listed in Table IV.

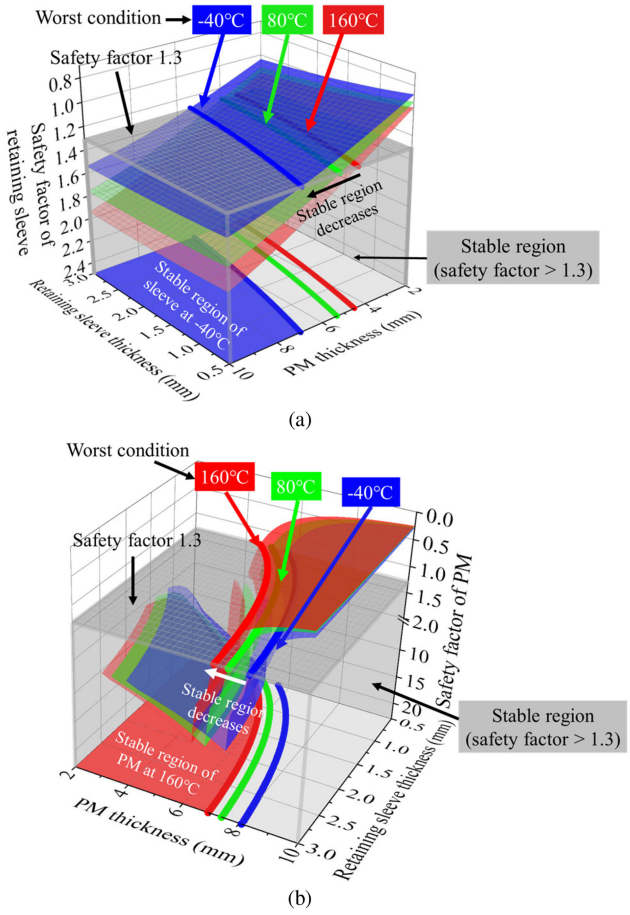

Fig. 4. Safety factor tendency according to the temperature at 126.5 krpm. (a) Retaining sleeve. (b) PM.

B. Stator Design

Based on the previously designed rotor in Section II-A, the stator was designed. For core material of the stator, 20PNF1500 is applied, and its thickness is 0.2 mm, the iron loss per kg is 15 W under the condition of magnetic flux density 1.0 T and frequency of 400 Hz. Considering the space in the given system, the stack length and the stator diameter were selected

$$\begin{bmatrix} A_{FE} \\ B_{FE} \\ A_{PM} \\ B_{PM} \\ A_S \\ B_S \end{bmatrix} = \begin{bmatrix} \frac{E_{FE}}{1-\nu_{FE}} & -\frac{E_{FE}}{1+\nu_{FE}}\cdot\frac{1}{r_1^2} & 0 & 0 & 0 & 0 \\ \frac{E_{FE}}{1-\nu_{FE}} & -\frac{E_{FE}}{1+\nu_{FE}}\cdot\frac{1}{r_2^2} & -\frac{E_{PM}}{1-\nu_{PM}} & \frac{E_{PM}}{1+\nu_{PM}}\cdot\frac{1}{r_2^2} & 0 & 0 \\ r_2 & \frac{1}{r_2} & -r_2 & -\frac{1}{r_2} & 0 & 0 \\ 0 & 0 & \frac{E_{PM}}{1-\nu_{PM}} & -\frac{E_{PM}}{1+\nu_{PM}}\cdot\frac{1}{r_3^2} & -\frac{E_S}{1-\nu_S} & \frac{E_S}{1+\nu_S}\cdot\frac{1}{r_3^2} \\ 0 & 0 & r_3 & \frac{1}{r_3} & -r_3 & -\frac{1}{r_3} \\ 0 & 0 & 0 & 0 & \frac{E_S}{1-\nu_S} & -\frac{E_S}{1+\nu_S}\cdot\frac{1}{r_4^2} \end{bmatrix}^{-1} \times \begin{bmatrix} \frac{3+\nu_{FE}}{8}\rho_{FE}r_1^2\omega^2 \\ \frac{3+\nu_{FE}}{8}\rho_{FE}r_2^2\omega^2 - \frac{3+\nu_{PM}}{8}\rho_{PM}r_2^2\omega^2 \\ (1-\nu_{FE}^2)\frac{\rho_{FE}r_2^3\omega^2}{8E_{FE}} - (1-\nu_{PM}^2)\frac{\rho_{PM}r_2^3\omega^2}{8E_{PM}} + r_2(C_{FE}-C_{PM})(T-T_0) \\ \frac{3+\nu_{PM}}{8}\rho_{PM}r_3^2\omega^2 - \frac{3+\nu_S}{8}\rho_S r_3^2\omega^2 \\ \delta + (1-\nu_{PM}^2)\frac{\rho_{PM}r_3^3\omega^2}{8E_{PM}} - (1-\nu_S^2)\frac{\rho_S r_3^3\omega^2}{8E_S} + r_2(C_{PM}-C_S)(T-T_0) \\ \frac{3+\nu_S}{8}\rho_S r_4^2\omega^2 \end{bmatrix} \quad (1)$$

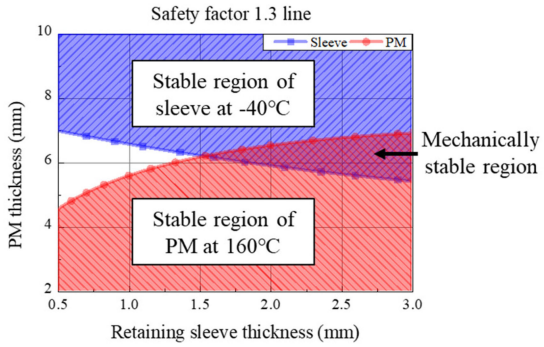

Fig. 5. Mechanically stable region.

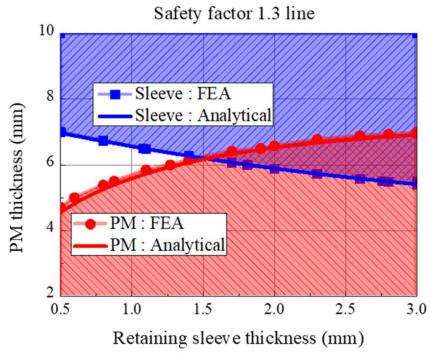

Fig. 6. Safety factor 1.3 line and mechanically stable region of PM and retaining sleeve calculated by FEA and analytical model.

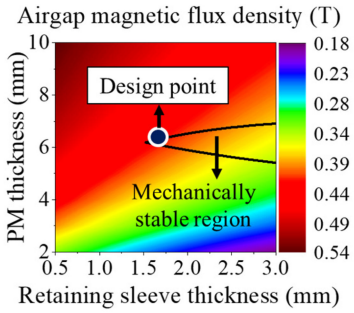

Fig. 7. Airgap magnetic flux density according to the rotor dimension, and rotor design point.

TABLE IV
SPECIFICATIONS OF THE DESIGNED ROTOR

Parameter	Value
Shaft inner radius (mm)	3.0
Shaft thickness (mm)	2.0
PM thickness (mm)	6.3
Retaining sleeve thickness (mm)	1.7
Interference (mm)	0.08
Safety factor of retaining sleeve	1.31 / 1.31 (analytical / FEA)
Safety factor of PM	1.40 / 1.40 (analytical / FEA)

as 44 mm and 108 mm. The current limit was determined as 42 A_{rms}, which included an additional margin while considering the instantaneous current, loss current, and sensor specifications of the inverter. The current density limit was 7 A_{rms}/mm^2 while considering the thermal characteristics of the motor system, and the DC link voltage was 350 V_{DC}. The maximum bare wire

TABLE V
REQUIREMENTS OF THE MOTOR

Parameter	Value
Stator core material	20PNF1500
Pole / slot number	2 / 6
Stator diameter (mm)	108.0
Stack length (mm)	44.0
Current (A_{rms})	42.0
Current density (A_{rms}/mm^2)	7.0
Maximum output power (kW)	14.4
Maximum rotational speed (krpm)	110
Maximum torque (Nm)	1.25

slot fill factor was assumed to be 40%. The requirements of the motor are summarized in Table V. When distributed winding is applied, there is an advantage that the eddy current loss of PM and retaining sleeve is smaller than that of the concentrated winding. However, the total motor size is increased because of the end coil height. Therefore, to minimize the motor size, a 2-pole 6-slot concentrated winding was chosen.

For SPMSMs comprising a ring-type PM, there is almost no difference between the d-axis inductance L_d and q-axis inductance L_q. Therefore, the torque can be expressed as follows:

$$T = p\left\{\sqrt{3}\lambda_m i\cos\beta + \frac{3}{2}(L_q - L_d)i^2\sin 2\beta\right\} \approx \frac{3ei}{\omega} \quad (2)$$

here, T is the torque, p is the pole pair number, λ_m is the no-load flux linkage, β is the current phase angle, i is the rms value of the current, e is the rms value of the phase back-electromotive force (BEMF), and ω is the rotational speed. When the maximum current within the constraints is used, which is 42 A_{rms}, the BEMF for satisfying the output power is determined to be 115 V_{rms}. Using SHA, which is explained in Section II-A, the BEMF per 1 turn was calculated for when the stack length is 44 mm at 110 kpm. Then, from the BEMF per 1 turn, the minimum number of turns that satisfies the target BEMF was determined to be 42 turns.

When using the maximum current and maximum current density within the constraints, which are 42 A_{rms} and 7 A_{rms}/mm^2, respectively, the cross-sectional area of the coil is determined as follows:

$$A_{coil} = \frac{i}{j \times a} \quad (3)$$

where A_{coil} is the cross-sectional area of coil, j is the rms value of the current density, and a is the number of parallel circuits. The number of series turns per phase and the slot area have the following relationship.

$$N = \frac{K_{wb}}{a \times m \times A_{coil}} \times s \times A_{slot} \quad (4)$$

Here, N is the number of series turns per phase, K_{wb} is the bare wire slot fill factor, m is the number of phases, s is the number of slots, and A_{slot} is the slot area. The slot area is determined by the number of series turns per phase, and there are several combinations of the tooth and yoke widths under the same slot area condition. The relationship between the magneto-motive

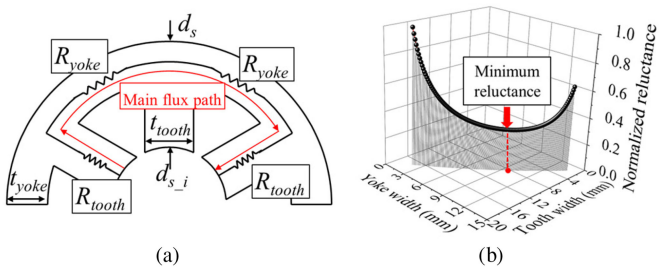

Fig. 8. Magnetic circuit and reluctance of two-pole six-slot SPMSM. (a) Magnetic circuit. (b) Reluctance according to tooth and yoke width.

force (MMF), reluctance, and magnetic flux is as follows:

$$Ni = R_m \Phi \tag{5}$$

where Ni is the MMF, R_m is the reluctance, and Φ is the magnetic flux. To maximize the magnetic flux at the same MMF, the reluctance must be minimized. Therefore, the width of the tooth and yoke were determined to minimize the reluctance. The main magnetic flux path of the two-pole six-slot is presented in Fig. 8(a). The reluctance of the tooth, yoke, and total reluctance of the magnetic circuit can be expressed as follows:

$$R_{tooth} = \frac{d_s - d_{s\_i} - t_{yoke}}{2\mu_0 \mu_r t_{tooth} l_{stk}}, \quad R_{yoke} = \frac{\pi}{6} \frac{d_s - t_{yoke}}{\mu_0 \mu_r t_{yoke} l_{stk}} \tag{6}$$

$$R_{total} = 2R_{yoke} + 2R_{tooth} \tag{7}$$

where R_{tooth} and R_{yoke} are the reluctance of the tooth and yoke, respectively, R_{total} is the total reluctance of the magnetic circuit, d_s is the stator outer diameter, d_{s_i} is the stator inner diameter, t_{tooth} is the tooth width, t_{yoke} is the yoke width, μ_r is the relative permeability, and l_{stk} is the stack length.

The relationship between the width of the tooth and yoke is expressed as follows.

$$t_{yoke} = \frac{d_s}{2} - \frac{t_{tooth} s}{\pi} - \sqrt{\left(\frac{t_{tooth} s}{\pi}\right)^2 + d_{s\_i}^2 + \frac{4A_{slot} s - 2d_{s\_i} t_{tooth} s}{\pi}} \tag{8}$$

Here, the tooth width and yoke width were calculated under the constant slot area condition, and the slot area was calculated from the maximum limit current and maximum current density conditions. The width of the tooth and yoke were determined as 8.0 mm and 9.8 mm, respectively, such that the reluctance of the magnetic circuit is minimized on substituting (8) into (6)–(7). The calculated reluctance according to the yoke and tooth width is presented in Fig. 8(b). Here, since the airgap reluctance does not depend on the shape of the stator, and is always a constant offset component, only the reluctance of the stator is considered. The parameters of the base model are summarized in Table VI, and the configuration of the base model is presented in Fig. 9.

III. Size Modification Using Analytical Approach

In the previous section, the base model was designed while considering the initial space of the system and power source specification. In this section, from the designed base model, the characteristics of the modified model were investigated by altering the size of the motor. In particular, the parameters and characteristics of the motor were calculated according to the SR and TD to determine the improved model, which is called the sizing model, with the maximum efficiency and a reduced eddy current loss within the constraint conditions such as the current density and DC link voltage. In this case, as the rotor was designed while considering mechanical stress, the cross section of the rotor was fixed. The size of the motor can then be represented by two independent variables: the SR and TD [16]. These variables are expressed as follows:

TABLE VI
Parameters of the Designed Base Model

Parameter	Value
Inner shaft radius (mm)	3.0
Shaft / PM / Sleeve thickness (mm)	2.0 / 6.3 / 1.7
Stator outer diameter (mm)	108.0
Stack length (mm)	44.0
Tooth / Yoke width (mm)	8.0 / 9.8
Number of series turns per phase	42
Phase current (A_{rms})	42.0

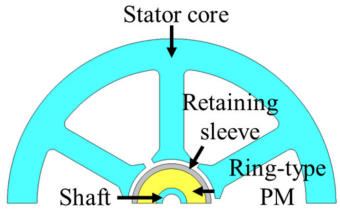

Fig. 9. Configuration of the base model.

$$\mathrm{SR} = \frac{l_{stk}}{d_r}, \quad \mathrm{TD} = \frac{4T_{\max}}{\pi d_s^2 l_{stk}} \tag{9}$$

where d_r is the rotor diameter, and $T_{\max}$ is the maximum torque. The SR and TD can be expressed as functions of the size related variables d_s, d_r, and l_{stk}, such that d_s and l_{stk} can also be expressed as functions of SR and TD. Therefore, the parameters and dimensions of the motor can be expressed as the independent variables SR and TD.

A. Motor Parameters

1) Armature Turns: The number of series turns per phase was calculated under the constant no-load BEMF condition. In order to obtain the constant no-load BEMF, the no-load flux linkage must be constant. Assuming that the rotor diameter and no-load flux linkage are constant, the number of series turns per phase of the modified model is expressed as follows.

$$N_{mo} \approx N_{base} \frac{l_{stk\_base}}{l_{stk\_mo}} \tag{10}$$

Here, the subscript "base" denotes the base model, and the subscript "mo" denotes the modified model.

2) Resistance and Inductance: On the assumption that the fill factor is constant, the phase resistance of the modified model

can be calculated as follows:

$$R_{a\_mo} \approx R_{a\_base} \frac{l_{coil\_mo} N_{mo} A_{slot\_base}}{l_{coil\_base} N_{base} A_{slot\_mo}} \tag{11}$$

where R_a is the resistance, and l_{coil} is the total length of the coil.

The d, q-axis inductance can be expressed as follows.

$$L_{d,q\_mo} = \frac{3}{\pi}\mu_0 \left(\frac{K_w N}{p}\right)^2 \frac{d_r l_{stk}}{g} \approx L_{d,q\_base} \frac{l_{stk\_mo} N_{mo}^2}{l_{stk\_base} N_{base}^2} \tag{12}$$

Here, L_{d,q_base} is the d, q-axis inductance of the initial model and is calculated using FEA, and K_w is the winding factor.

3) Losses: As ultra-high-speed motors have a large eddy current loss in PM and retaining sleeve, this should be considered when designing the motor. For a conducting body with thickness c, height h, and length l, the eddy current loss is expressed as follows [19].

$$W_{eddy} \propto \frac{c^3 hl}{\rho} \left(\frac{dB}{dt}\right)^2 \tag{13}$$

In reality, at very high frequencies, the eddy current loss is not exactly proportional to the square of the frequency due to the skin effect. However, in this study, since the trend of the eddy current loss according to the shape change of the motor was predicted analytically under the same frequency condition, it is assumed that the difference in skin effect according to the shape change is negligible. Then, the frequency term can be eliminated, so the sizing equation was derived based on (13).

As the cross section of the rotor is fixed and only the axial length is changed, the eddy current loss of the PM and retaining sleeve is proportional to the stack length l_{stk}. The magnetic flux density can be divided into that caused by the PM field and that caused by the armature current. The magnetic flux density caused by the armature current is proportional to the MMF of the armature current, and the eddy current loss of PM and retaining sleeve of the modified model can be expressed as follows.

$$W_{eddy\_mo}^{PM} \approx W_{eddy\_PM\_base}^{PM} \frac{l_{stk\_mo}}{l_{stk\_base}} + W_{eddy\_arm\_base}^{PM} \frac{l_{stk\_mo} N_{mo}^2 i_{mo}^2}{l_{stk\_base} N_{base}^2 i_{base}^2} \tag{14}$$

$$W_{eddy\_mo}^{sleeve} \approx W_{eddy\_PM\_base}^{sleeve} \frac{l_{stk\_mo}}{l_{stk\_base}} + W_{eddy\_arm\_base}^{sleeve} \frac{l_{stk\_mo} N_{mo}^2 i_{mo}^2}{l_{stk\_base} N_{base}^2 i_{base}^2} \tag{15}$$

Here, $W^{PM}{}_{eddy}$ and $W^{sleeve}{}_{eddy}$ indicate the eddy current loss of PM and retaining sleeve, respectively. The eddy current loss caused by the armature current ($W_{eddy\_arm\_base}$) and PM field ($W_{eddy\_PM\_base}$) were calculated using the following steps through a 3D FEA. Here, elements of the 3D FEA model was divided in consideration of the skin depth of PM and retaining sleeve [20]. Also, if the time step is not set small enough, the effects of the slot harmonic cannot be properly considered. Therefore, in consideration of the number of slots of the motor, the time step was set small enough to properly consider the slot harmonics, and the analysis was performed until the eddy current loss converged.

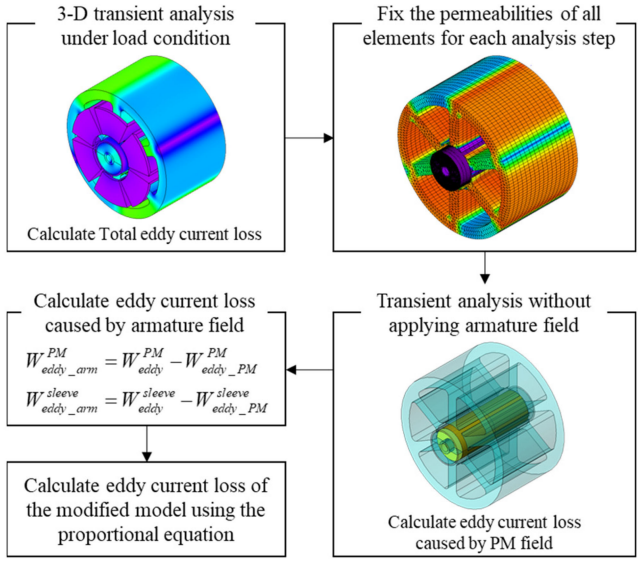

Fig. 10. Calculation process of rotor eddy current loss using 3D FEA and proportional equation.

1) 3D transient analysis was performed under the load condition, and the permeabilities of all elements for each analysis step were obtained.
2) The permeabilities of all elements for each analysis step were set to the value obtained from the aforementioned load condition.
3) The transient analysis was performed without applying armature field to obtain the eddy current loss caused by the PM field.
4) The eddy current loss caused by the armature field was calculated by subtracting the eddy current loss caused by the PM field from the total eddy current loss.

This eddy current loss calculation process is shown in Fig. 10. The eddy current loss obtained using this method was verified through 3D FEA for the sizing model, in Section III-C.

The iron loss of the stator core was obtained using 2D FEA as it has a large nonlinearity. Iron loss calculation process is shown in Fig. 11, which is described in detail as follows [21].

1) Radial and tangential component of the magnetic flux density at each mesh is calculated for one electrical angle period by using nonlinear 2D FEA.
2) From the magnetic flux density obtained in 1, magnitude of the fundamental and harmonic components is calculated by using Fourier transform.
3) From the iron loss data, the iron loss corresponding to the frequency and magnetic flux density of each harmonic is calculated.
4) Then, by summing iron loss of all harmonic components, iron loss of each mesh is calculated.
5) Finally, total iron loss is calculated by summing iron loss of each mesh, which was determined in 4.

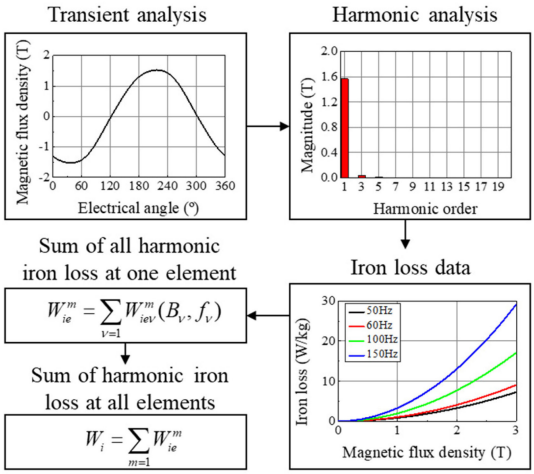

Fig. 11. Iron loss calculation process.

From the aforementioned process, the iron losses according to the SR and TD were calculated, and iron loss map was obtained using cubic spline interpolation.

The windage loss was calculated based on [22], as follows:

$$W_{windage} = \pi C_d \rho_{air} r_{sleeve}^4 \omega^3 l_{stk} \tag{16}$$

where $W_{windage}$ is the windage loss, C_d is the drag coefficient, ρ_{air} is the air density, and r_{sleeve} is the radius of the retaining sleeve. As the cross section of the rotor was fixed, r_{sleeve} remained constant and only l_{stk} changed. Therefore, the windage loss of the modified model was expressed as follows:

$$W_{windage\_mo} \approx W_{windage\_base} \frac{l_{stk\_mo}}{l_{stk\_base}} \tag{17}$$

In addition, in this study, an air foil bearing was applied which is oil-free and has a smaller size than a magnetic bearing that requires an additional control system. In general, the loss of air foil bearing is relatively small, so the bearing loss was neglected.

B. Constraint Considering First Bending Critical Speed

When the axial length of the rotor increases, the first bending critical speed decreases. If the rotor rotates at the critical speed, not only are vibration and noise generated, but a severe failure can also occur. Therefore, the maximum rotational speed of the motor should be designed such that it is below the first bending critical speed.

To find the maximum stack length that does not exceed the first bending critical speed, the frequency of the first bending critical speed was obtained via 3D FEA for a different stack length at rotational speed of 126.5 krpm, which includes a 15% additional margin over the maximum operating rotational speed. Considering a safety factor of 1.5 at 126.5 krpm, the frequency of the first bending critical speed should be greater than 3163Hz. Therefore, the maximum stack length was determined to be 56 mm, as shown in Fig. 12. Fig. 13 shows the Campbell diagram and first, second, and third bending mode with a stack length of 56 mm, and it was confirmed that there is no critical speed in the driving range.

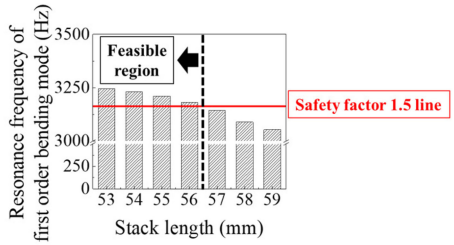

Fig. 12. Frequency of the first bending critical speed according to the stack length.

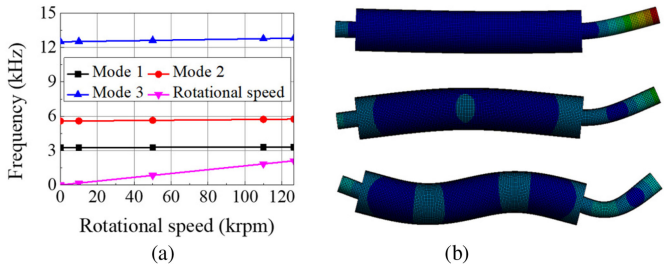

Fig. 13. Campbell diagram and bending mode at stack length 56 mm. (a) Campbell diagram. (b) First, second, and third bending mode.

C. Size Determination

The sizing model was determined to have the highest efficiency with a reduced eddy current loss while considering the constraints, as shown in Fig. 14. Since there are only two variables, SR and TD, and there was a maximum efficiency design point within the constraint conditions, the optimization theory was not applied. Here, the current density and line to line voltage are the constraints which should be lowered than 7 A_{rms}/mm^2 and 247.5 V_{rms}, respectively. Furthermore, as mentioned earlier, the stack length should be lower than 56 mm while considering the first bending critical speed. The design result of the sizing model is presented in Table VII, and configuration of the base model and sizing model are presented in Fig. 15. As shown in Table VII, the efficiency improved 0.3%p from 95.2% to 95.5%, and the eddy current loss decreased 17.5% from 317.0 W to 261.5 W. Also, eddy current loss calculation method is verified that the error of eddy current loss between the analytical result and 3D FEA result was only 0.57%.

IV. Design Results and Verification

A. Experimental Results

The prototype of the designed model was fabricated and verified via no-load and load tests. Fig. 16 presents the rotor, stator, and assembly of the prototype, and Fig. 17 shows the test setup. During the load test, water cooling was performed through the axial cooling channel of the housing, and the rotor cooling was performed by forced air-cooling through the air tube inside the hollow shaft. First, under the 1000 rpm condition at the ambient temperature, the no-load test was performed to measure the BEMF. Fig. 18(a) shows the no-load BEMF obtained via the no-load test and FEA. The error of the BEMF fundamental wave is 4.8%, which is acceptable. Then, the performance under the

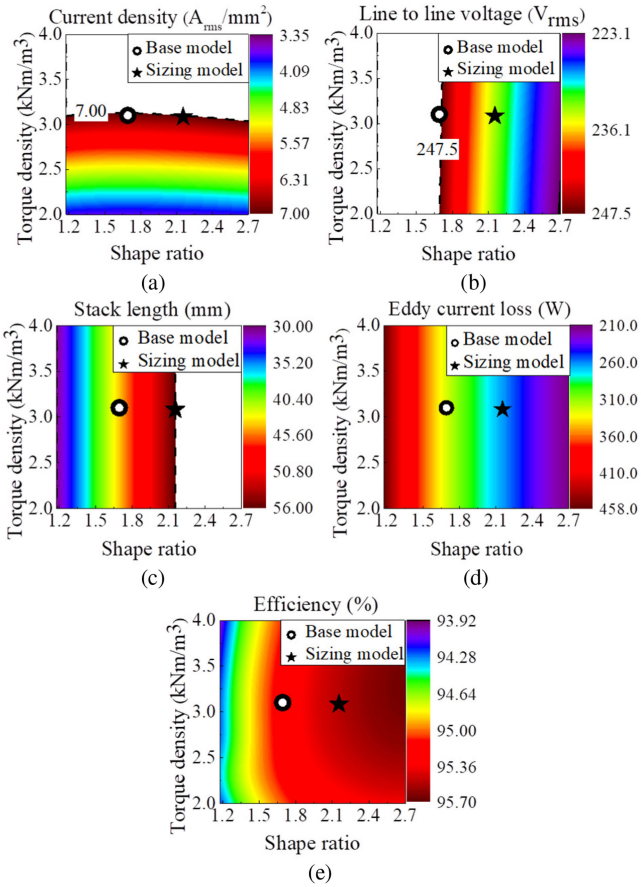

Fig. 14. Sizing effect according to the SR and TD. (a) Current density. (b) Line to line voltage. (c) Stack length. (d) Eddy current loss. (e) Efficiency.

TABLE VII
DESIGN RESULTS OF BASE MODEL AND SIZING MODEL

Parameter	Base model	Sizing model	
		Analytical result	FEA result
Rotational speed (krpm)	110	110	
Torque (Nm)	1.25	1.25	
Output power (kW)	14.4	14.4	
Stator diameter (mm)	108.0	96.0	
Stack length (mm)	44.0	56.0	
Rotor diameter (mm)		26.0	
Airgap length (mm)		1.4	
PM thickness (mm)		6.3	
Retaining sleeve thickness (mm)		1.7	
Stator core mass (kg)	1.52	1.49	
Stator copper mass (kg)	1.09	0.95	
PM mass (kg)	0.12	0.15	
Retaining sleeve mass (kg)	0.047	0.060	
Shaft mass (kg)	0.017	0.022	
Tooth / Yoke width (mm)	8.0 / 9.8	7.0 / 8.6	
Current density (A_{rms}/mm^2)	6.73	6.76	6.82
Number of series turns per phase	42	33	
PM eddy current loss (W)	61.4	51.4	51.1
Sleeve eddy current loss (W)	255.6	211.6	210.4
Stator core iron loss (W)	223.8	242.7	243.1
Copper loss (W)	148.0	132.4	131.9
Windage loss (W)	32.4	41.2	
Efficiency (%)	95.2	95.5	95.5
Shape ratio	1.692	2.154	
Torque density (kNm/m^3)	3.101	3.083	

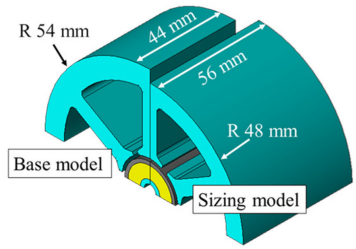

Fig. 15. 3D configuration of the base model and sizing model.

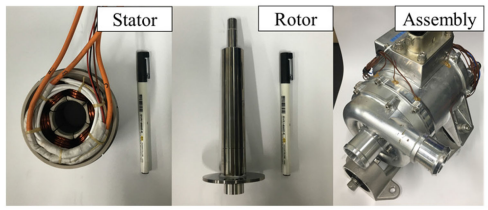

Fig. 16. Prototype.

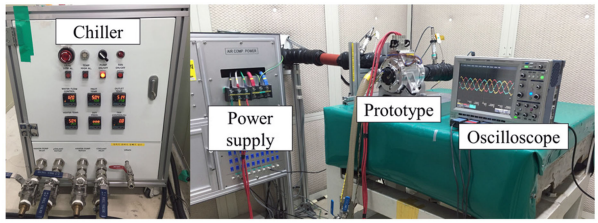

Fig. 17. Test setup.

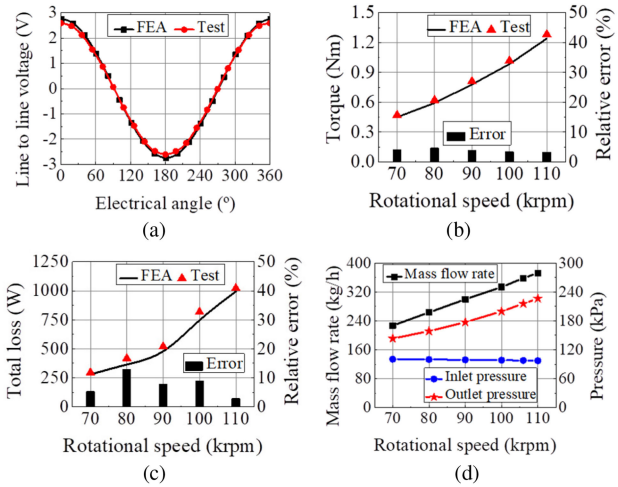

Fig. 18. Test and FEA results. (a) BEMF. (b) Torque. (c) Total loss. (d) Mass flow rate and pressure of air.

load condition such as torque and loss of the motor was measured through the centrifugal compressor system test. Although it is preferable to measure the torque directly in the dynamo set using a torque sensor, it was practically difficult to prepare the torque sensor available at high speed of 110 krpm. Thus, the torque was indirectly estimated by the following method. First, BEMF constant was calculated using the BEMF obtained through the no-load test. Then, the torque constant was calculated using the relational equation between the BEMF constant and the torque

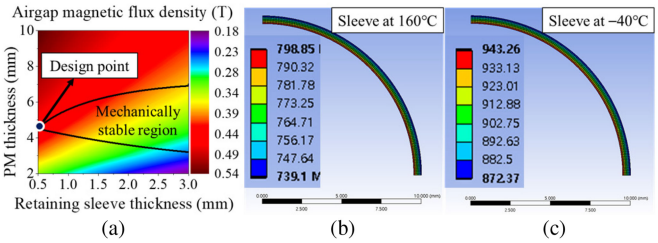

Fig. 19. (a) Rotor design point without considering worst condition. (b) Von-Mises stress of retaining sleeve at 160 °C. (c) Von-Mises stress of retaining sleeve at −40 °C.

constant. Finally, the test torque was estimated by multiplying the input current and the torque constant. Here, the input current was measured using an oscilloscope through the load test of the compressor system. The total loss of the motor was obtained by subtracting the estimated mechanical output power from the active power measured by the power analyzer. Fig. 18(b) and Fig. 18(c) shows the torque and total loss obtained via the load test and FEA, respectively. Here, FEA was conducted using the test load current. Also, to make a 3D FEA similar to the prototype, 3D FEA model was built by modelling the additional rotor core in the axial direction, which can make leakage flux pass. It is shown that the relative errors between the test torque and FEA torque are all below 4.6%, which is agreeable. The total loss obtained from test and FEA shows a maximum error of 12.7%. It is also acceptable since in the actual system, bearing loss and additional loss due to temperature rise in coil and PM can occur, which leads to the difference between the test loss and FEA loss. Also, the performance of the compressor system was confirmed by measuring the mass flow rate and pressure of the air, as shown in Fig. 18(d). In addition, the proposed design process was verified that the motor can be operated without mechanical failure at the maximum speed of 110 krpm.

B. Effectiveness of the Proposed Rotor Design Process

To verify the effectiveness of the proposed rotor design process presented in this paper, another rotor is designed without reflecting the worst conditions for each material. Generally, rotor is designed only considering the rotor stress at the operating temperature [9], which will be called conventional design in this paper. Thus, the rotor is designed so that the safety factor of the PM and retaining sleeve is equal to or greater than 1.3 at 160 °C, 126.5 krpm, which includes 15% additional margin. As shown in Fig. 19(a), the rotor is designed at the point of maximum airgap magnetic flux density. Fig. 19(b), (c) shows the von-Mises stress of the retaining sleeve at temperature of 160 °C and −40 °C, respectively. As shown in Fig. 19(c), maximum von-Mises stress is 943.26 MPa and safety factor of the retaining sleeve is 1.10 at −40 °C, which does not satisfy the target safety factor. At operating condition and worst condition, as listed in Table VIII, the safety factor of the designed rotor with proposed design process, which was explained in Section-II-A., and with conventional design process is summarized in Table IX. As can be seen from Table IX, safety factor of sleeve at worst condition of conventional design model is 1.10, while proposed design model is 1.31. This result shows that the proposed process provides more mechanically stable rotor design than the conventional method.

TABLE VIII
OPERATING AND WORST CONDITION OF EACH MATERIAL

Condition	Material	Speed (krpm)	Temperature (°C)
Operating	Sleeve, PM	110.0	160
Worst	Sleeve	126.5	-40
	PM	126.5	160

TABLE IX
SAFETY FACTOR OF DESIGNED ROTOR

Parameter	Condition	Proposed design	Conventional design
Safety factor of sleeve	Operating	1.64	1.32
	Worst	1.31	1.10
Safety factor of PM	Operating	15.0	2.95
	Worst	1.40	1.35

V. CONCLUSION

The design of the two-pole six-slot 14.4 kW, 110 krpm ultra-high-speed SPMSM for a FCEV compressor was presented. First, the design of the base model was conducted while considering the mechanical stress and no-load airgap flux density using an analytical method. The safety factor of PM and retaining sleeve according to the temperature were calculated, and the worst condition of each material was determined. It was figured out that for brittle material PM, as temperature increased, mechanically stable region decreased, and for ductile material retaining sleeve, mechanically stable region decreased as temperature decreased. From the characteristics of the base model calculated using FEA, the characteristics including the rotor eddy current loss according to the changes in the TD and SR were determined using the proportional equation. The eddy current loss tended to decrease as SR increased, but there was a trade off relationship that critical speed decreased as SR increased. Therefore, SR and TD of the sizing model were determined with reduced eddy current loss while satisfying critical speed limit condition. Finally, the sizing model was fabricated and tested for verification. The test result and FEA result of torque and total loss were then compared, and it was confirmed that the maximum error of the torque and total loss were less than 4.6% and 12.7%, respectively. Furthermore, it was verified that the designed model can rotate without failure at a maximum speed of 110 krpm through test. In addition, effectiveness of the proposed rotor design method was validated by comparing conventional method and proposed method design result. It was confirmed that the rotor designed by the conventional design process did not meet the target safety factor, which considers mechanical stress at high temperature only.

REFERENCES

[1] J. Snoussi, S. B. Elghali, M. Benbouzid, and M. F. Mimouni, "Optimal sizing of energy storage systems using frequency-separation-based energy management for fuel cell hybrid electric vehicles," *IEEE Trans. Veh. Technol.*, vol. 67, no. 10, pp. 9337–9346, Oct. 2018.

[2] D. Zhao, F. Gao, D. Bouquain, M. Dou, and A. Miraoui, "Sliding-mode control of an ultrahigh-speed centrifugal compressor for the air management of fuel-cell systems for automotive applications," *IEEE Trans. Veh. Technol.*, vol. 63, no. 1, pp. 51–61, Jan. 2014.
[3] D. Zhao, B. Blunier, F. Gao, M. Dou, and A. Miraoui, "Control of an ultrahigh-speed centrifugal compressor for the air management of fuel cell systems," *IEEE Trans. Ind. Appl.*, vol. 50, no. 3, pp. 2225–2234, May/Jun. 2014.
[4] M. S. Lim, S. H. Chai, J. S. Yang, and J. P. Hong, "Design and verification of 150-krpm PMSM based on experiment results of prototype," *IEEE Trans. Ind. Electron.*, vol. 62, no. 12, pp. 7827–7836, Dec. 2015.
[5] F. Zhang, R. Dai, G. Liu, and T. Cui, "Design of HSIPMM based on multi-physics fields," *IET Electric Power Appl.*, vol. 12, no. 8, pp. 1098–1103, Sep. 2018.
[6] F. Cupertino, R. Leuzzi, V. G. Monopoli, and G. L. Cascella, "Maximisation of power density in permanent magnet machines with the aid of optimisation algorithms," *IET Electric Power Appl.*, vol. 12, no. 8, pp. 1067–1074, Sep. 2018.
[7] S. M. Barrans, M. M. J. Al-Ani, and J. Carter, "Mechanical design of rotors for permanent magnet high-speed electric motors for turbocharger applications," *IET Electric Syst. Transp.*, vol. 7, no. 4, pp. 278–286, Dec. 2017.
[8] J. Ahn, C. Han, C. Kim, and J. Choi, "Rotor design of high-speed permanent magnet synchronous motors considering rotor magnet and sleeve materials," *IEEE Trans. Appl. Supercond.*, vol. 28, no. 3, pp. 1–4, Apr. 2018.
[9] F. R. Ismagilov, N. Uzhegov, V. E. Vavilov, V. I. Bekuzin, and V. V. Ayguzina, "Multidisciplinary design of ultra-high-speed electrical machines," *IEEE Trans. Energy Convers.*, vol. 33, no. 3, pp. 1203–1212, Sep. 2018.
[10] L. Li, W. Li, D. Li, X. Zhang, and Y. Fan, "Influence of sleeve thickness and various structures on eddy current losses of rotor parts and temperature field in surface mounted permanent-magnet synchronous motor," *IET Electric Power Appl.*, vol. 12, no. 8, pp. 1183–1191, Sep. 2018.
[11] D. Krähenbühl, C. Zwyssig, H. Weser, and J. W. Kolar, "A miniature 500 000-r/min electrically driven turbocompressor," *IEEE Trans. Ind. Appl.*, vol. 46, no. 6, pp. 2459–2466, Nov./Dec. 2010.
[12] Z. Huang and Y. Le, "Rotordynamics modelling and analysis of high-speed permanent magnet electrical machine rotors," *IET Electric Power Appl.*, vol. 12, no. 8, pp. 1104–1109, 2018.
[13] P. D. Pfister and Y. Perriard, "Very-high-speed slotless permanent-magnet motors: Analytical modeling, optimization, design, and torque measurement methods," *IEEE Trans. Ind. Electron.*, vol. 57, no. 1, pp. 296–303, Jan. 2010.
[14] Z. Huang and J. Fang, "Multiphysics design and optimization of high-speed permanent-magnet electrical machines for air blower applications," *IEEE Trans. Ind. Electron.*, vol. 63, no. 5, pp. 2766–2774, Sep. 2016.
[15] N. Uzhegov, E. Kurvinen, J. Nerg, J. Pyhonen, J. T. Sopanen, and S. Shirinskii, "Multidisciplinary design process of a 6-Slot 2-Pole high-speed permanent-magnet synchronous machine," *IEEE Trans. Ind. Electron.*, vol. 63, no. 2, pp. 784–795, Feb. 2016.
[16] H. J. Kim, J. S. Jeong, M. H. Yoon, J. W. Moon, and J. P. Hong, "Simple size determination of permanent-magnet synchronous machines," *IEEE Trans. Ind. Electron.*, vol. 64, no. 10, pp. 7972–7983, Oct. 2017.
[17] J. Shigley, C. Mischke, and R. Budynas, *Mechanical Engineering Design*. New York, NY, USA: McGraw-Hill, 2006.
[18] K. H. Shin, H. W. Cho, K. H. Kim, K. Hong, and J. Y. Choi, "Analytical investigation of the on-load electromagnetic performance of magnetic-geared permanent-magnet machines," *IEEE Trans. Magn.*, vol. 54, no. 11, pp. 1–5, Nov. 2018.
[19] H. W. Jun, J. Lee, H. W. Lee, and W. H. Kim, "Study on the optimal rotor retaining sleeve structure for the reduction of eddy-current loss in high-speed SPMSM," *IEEE Trans. Magn.*, vol. 51, no. 3, pp. 1–4, Mar. 2015.
[20] D. M. Kim, J. H. Kim, S. G. Lee, M. R. Park, G. H. Lee, and M. S. Lim, "Estimation method for rotor eddy current loss in ultra-high-speed surface-mounted permanent magnet synchronous motor," *IEEE Trans. Magn.*, vol. 57, no. 2, pp. 1–5, Feb. 2021.
[21] S. H. Park, J. C. Park, S. W. Hwang, J. H. Kim, and M. S. Lim, "Suppression of torque ripple caused by misalignment of the gearbox by using harmonic current injection method," *IEEE/ASME Trans. Mechatronics*, vol. 25, no. 4, pp. 1990–1999, Aug. 2020.
[22] J. Vrancik, "Prediction of windage power loss in alternators," *NASA*, WA, DC, 1968.

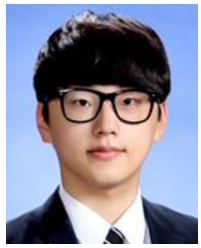

Jae-Hyun Kim received the bachelor's degree in mechanical engineering, in 2017, from Hanyang University, Seoul, South Korea, where he is currently working toward the Ph.D. degree in automotive engineering. His research interests include the design, and the analysis of vibration and noise of electric machines.

Dong-Min Kim (Member, IEEE) received the B.S. degree in electronic system engineering, and the Ph.D. degree in automotive engineering from Hanyang University, Seoul, South Korea, in 2013 and 2021, respectively.

In 2021, he was a Postdoctoral Researcher with Hanyang University, Seoul, South Korea. Since 2021, he has been with Honam University, Gwangju, South Korea, where he is currently an Assistant Professor. His research interests include design optimization of electric machines for automotive and industrial applications, modeling and optimization of electric vehicles, hybrid electric vehicles, and fuel cell electric vehicles.

Young-Hoon Jung received the bachelor's degree in mechanical engineering, the integrated master's and the Ph.D. degrees in automotive engineering from Hanyang University, Seoul, South Korea, in 2013 and 2020, respectively. Since 2020, he has been with R&D Division, Hyundai Motor Company, Hwaseong, South Korea, where he is currently a Senior Research Engineer. His research interests include electric machine design for automotive and robot applications, and ultra-high speed motors.

Myung-Seop Lim received the bachelor's degree in mechanical engineering, the master's degree in automotive engineering, and the Ph.D. degree in automotive engineering from Hanyang University, Seoul, South Korea, in 2012, 2014, and 2017, respectively.

From 2017 to 2018, he was a Research Engineer with Hyundai Mobis, Yongin, South Korea. From 2018 to 2019, he was an Assistance Professor with Yeungnam University, Daegu, South Korea. Since 2019, he has been with Hanyang University, Seoul, South Korea, where he is currently an Assistant Professor.

His research interests include electromagnetic field analysis and multi-physics analysis of electric machinery for mechatronics systems such as automotive and robot applications.